Lab on a Chip

PAPER

View Article Online
View Journal



Cite this: DOI: 10.1039/d6lc00382f

# Adeno-associated viral vector purification using a centrifugal microfluidic system: towards workflow automation for low-volume sample processing

Matthias Geissler, *[ab] Lidija Malic, [ab] Liviu Clime, [ab] Dillon Da Fonte,[ab] Christina Nassif,[ab] Mojra Janta-Polczynski, [ab] Caroline Miville-Godin,[ab] Daniel Brassard, [ab] Nasha Nassoury,[c] Richard Gingras,[c] Nazila Nazemi-Moghaddam,[c] Parminder Singh Chahal,[c] Rénald Gilbert [c] and Teodor Veres [ab]

This paper describes the development of an integrated assay for the purification of adeno-associated virus (AAV) particles from crude lysate using a microfluidic cartridge and a centrifugal platform that enables pneumatic actuation of liquids during rotation. The cartridge features POROS™ CaptureSelect™ AAVX Affinity Resin as a solid-phase extraction (SPE) matrix and a layout that is compatible with workflow automation and low-volume sample processing. The integrated process takes ~30 to 60 min depending on the input volume and comprises 22 consecutive steps, starting with crude lysate and ending with an AAV sample conditioned for downstream analysis or long-term storage. Numerical simulations, conducted as part of the design validation, reveal uniform flow across the SPE matrix for both in-plane and out-of-plane orientations. The performance of the system is demonstrated using AAV8 with volumes ranging from 50 to 500 µL. The on-chip purification process generally shows higher extraction efficiency than a benchmark procedure performed manually using spin columns. The capacity to remove plasmid DNA is validated using samples with calibrated spike-in concentration that were analyzed by qPCR, suggesting depletion of >99.99%. Biological activity of purified AAV particles was assessed in a transduction assay involving human embryonic kidney cells and recombinant AAV2 expressing green fluorescent protein. The platform's compatibility with low-volume production addresses gaps in current gene therapy manufacturing pipelines, underscoring its potential to streamline quality assurance protocols, reduce manual intervention, and accelerate scalable AAV production.

Received 6th May 2026,
Accepted 24th May 2026

DOI: 10.1039/d6lc00382f

rsc.li/loc



## 1 Introduction

Adeno-associated viral (AAV) vectors[1–3] have emerged as transformative tools in many areas of biomedical research due to the unique properties that these particles provide. AAV vectors are used to deliver genetic material into cells with high efficiency, which has become a cornerstone of modern therapeutic strategies.[4] This approach is being employed for the treatment of several disorders which include eye diseases, haemophilia and muscular dystrophy.[2] Moreover, AAV vectors play a crucial role in the study of gene function and the delivery of CRISPR components to cells or tissues for precise gene editing. Several AAV-based therapies have been approved by the FDA given the safety profile that these vectors exhibit and their ability to sustain long-term expression in non-dividing cells, underscoring their therapeutic potential.[2] A common method for producing AAV is plasmid-based transfection,[5,6] a multi-step process that involves plasmid preparation and cell culture, followed by cell lysis and purification of the viral particles.

Quality control is important in AAV vector production processes to ensure product consistency, safety, and efficacy.[7,8] Prior to downstream processing, it is important to determine the concentration of AAV particles in the crude lysate which also contains residual unutilized plasmid DNA encoding the same sequence as the gene of interest. If analyzed by qPCR or ddPCR, these samples may significantly overestimate titers due to the presence of plasmid DNA. The purification process is commonly performed using affinity chromatography with capture ligands covalently linked to microparticles serving as a solid-phase

[a] Medical Devices Research Centre, National Research Council of Canada, 75 de Mortagne Boulevard, Boucherville, QC, J4B 6Y4, Canada.
E-mail: matthias.geissler@cnrc-nrc.gc.ca
[b] Centre for Research and Applications in Fluidic Technologies, Department of Mechanical and Industrial Engineering, 5 King's College Road, Toronto, ON, M5S 3G8, Canada
[c] Human Health Therapeutics Research Centre, National Research Council of Canada, 6100 Royalmount Avenue, Montreal, QC, H4P 2R2, Canada

extraction (SPE) matrix.[8–10] Several affinity capture resins are commercially available, which include POROS™ CaptureSelect™ AAVX Affinity Resin (Thermo Fisher Scientific), AVB Sepharose High Performance and Capto AVB (both from Cytiva), and AVIPure® AAV Affinity Resin (Repligen).[9] Resin is packed inside a chromatography column, typically designed for processing relatively large sample volumes ranging from 5 mL to 6.3 liters. In early-stage research and development, however, only small amounts of viral vector can be available for testing, making low-volume purification essential. The well-established ultracentrifugation method,[11–13] which uses multilayered iodixanol gradients of varying concentrations, separates plasmids from AAV particles based on differences in their densities and is particularly suitable for small-volume purification (*e.g.*, 1–10 mL). However, this step is lengthy (4–5 h) and labor-intensive, therefore representing a bottleneck for high-throughput screening. Moreover, ultracentrifugation is not compatible with very low volumes (*e.g.*, <1 mL) that might be available in research when optimizing for efficiency, scalability, and purity. Emerging methods based on microfluidics promise to provide a plausible, technologically convenient way of integrating and automating purification protocols at this scale.[14–16] These systems offer improved reproducibility, reduced hands-on time, and compatibility with low-volume inputs—features increasingly critical for translational research and decentralized biomanufacturing.

Centrifugal microfluidics, commonly referred to as lab-on-a-disk technology, leverages rotation-induced forces to manipulate small volumes of liquid in microstructured devices.[14,17] The centrifugal force field ($\vec{F}_{cf}$) generated by a spinning disk drives liquid radially outward, enabling downstream transfer without external pumps or complex instrumentation. Moreover, centrifugation makes it possible to remove unwanted air bubbles from the fluidic circuit and reduce dead volumes to negligible levels. By implementing geometric control elements, such as capillary valves, burst valves, or siphon valves, specific unit operations that include liquid dispensing, mixing, splitting or metering can be programmed into the disk's architecture.[14] This programmability enables precise control of sample and reagent handling without operator intervention. A particularly impactful application of centrifugal microfluidics is sample preparation for chemical, biological, and clinical assays[18–23]—a step that is traditionally labor-intensive and can largely influence analytical outcomes. For example, Duffy *et al.* have implemented silica and carbon monolithic columns on a rotating disk to purify and pre-concentrate analytes (such as phenol from tap water) for on-chip detection using UV/vis spectrophotometry.[22] Zhao *et al.* have removed proteins and lipids from serum using centrifugal segregation to deliver cleaned analyte fractions for surface-assisted laser desorption/ionization–mass spectrometry (MS).[20] Futami *et al.* have performed whole blood processing on a rotating platform, coupling methanol-induced protein precipitation with SPE to produce samples suitable for small-molecule analysis using electrospray ionization MS.[18] Strohmeier *et al.* have used magnetic nanoparticles to extract nucleic acids deriving from microbial organisms and whole blood with the help of permanent magnets implemented on their platform.[23] Despite these technical advancements, achieving fully integrated and automated multi-step workflows remains challenging.

Herein, we describe a centrifugal system enabling purification of AAV vectors from small sample volumes (Fig. 1) using POROS™ CaptureSelect™ AAVX Affinity Resin. The process starts with crude lysate and ends with a purified AAV sample suited for long-term storage, downstream analysis, or use in cell transduction assays (Fig. 1a). The microfluidic cartridge is operated on a platform equipped to actuate fluids pneumatically during rotation.[24–27] The capacity of this platform to automate complex sample preparation procedures has been demonstrated previously for the extraction and purification of DNA from whole blood using a glass microfiber-based SPE matrix,[26] the preparation of adaptor-ligated libraries for DNA sequencing,[28] and the isolation of extracellular vesicles from plasma using size-based filtration and immunomagnetic capture.[29] Moreover, we have shown its compatibility with ddPCR workflows,[30,31] potentially enabling AAV purification to be integrated in a sample-to-answer format. We therefore believe the system presented here could possibly evolve toward a companion tool for quality control in AAV manufacturing processes.

# 2 Materials and methods

## 2.1 Reagents

POROS™ CaptureSelect™ AAVX Affinity Resin was purchased from Thermo Fisher Scientific (Waltham, MA). The composition of buffer solutions is provided in Table S1.

## 2.2 Cartridge fabrication

Fluidic structures (Fig. S1 and S2, Table S2) were machined (Q350 CNC Mill; Menig Automation, Morgan Hill, CA) into a polycarbonate (PC) block (4.5 mm in thickness; McMaster-Carr, Elmhurst, IL) following previously established procedures.[30,32] The fluidic circuit was enclosed using double-sided adhesive (ARclear 93495, 41 μm in thickness; Adhesives Research, Glen Rock, PA) applied to a thin PC sheet (125 μm in thickness; AGC, Tokyo, Japan). Metal connectors (0.036″ OD; New England Small Tube Corporation, Litchfield, NH) were inserted in their respective holes and fixed using UV-curable glue (Vitralit® UV 2114; Panacol, Torrington, CT). The capture unit was produced by hot embossing (EVG 520 system; EV Group, St. Florian am Inn, Austria) in Mediprene OF 400M (HEXPOL TPE, Malmö, Sweden) using conditions described elsewhere.[24,33] 100 μL of bead slurry diluted 1 : 10 (v/v) in 0.1 M NaCl solution (Sigma-Aldrich, St. Louis, MO) was pipetted into the filling port to form a densely packed extraction matrix inside the capture chamber (Fig. S3). Once filled, the capture unit was glued to the cartridge using double-sided adhesive. The top surface of the capture unit was covered with Zeonor film (ZF14-188; Zeon Chemicals, Louisville, KY) to seal the filling port and prevent deformation of the chamber during operation. 1.5 mL micro tubes (Sarstedt,

 

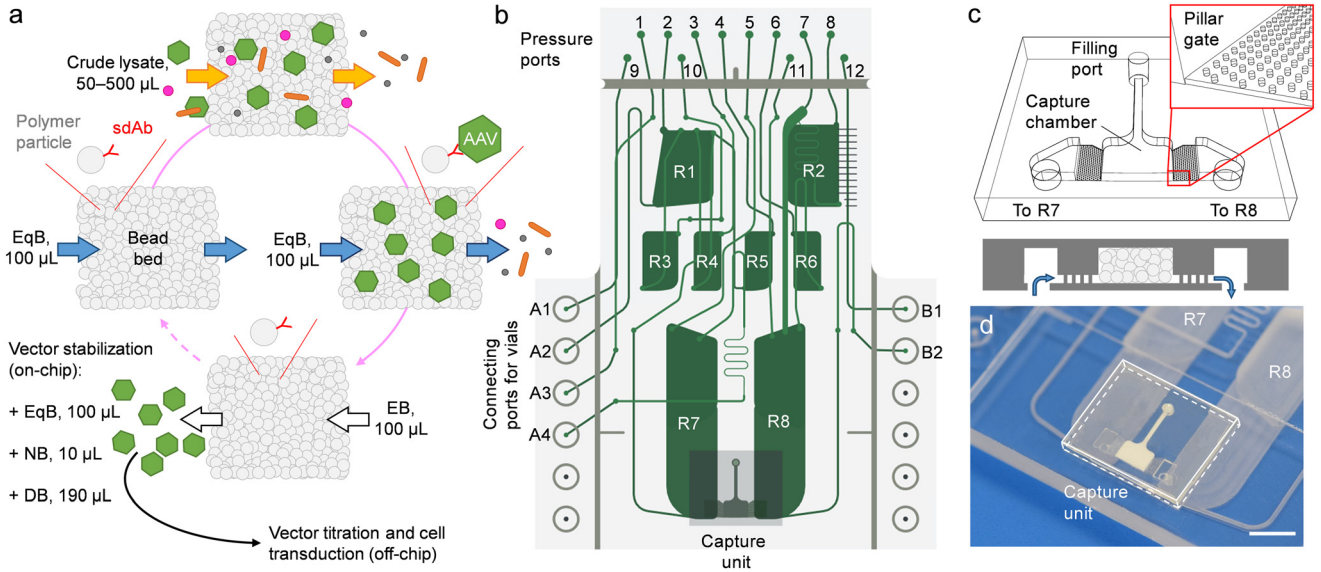


**Fig. 1** Implementation of affinity-based AAV purification. (a) Schematic illustration of the processing steps conducted on the cartridge. Bead slurry is conditioned using EqB. Lysate is then flown through the capture chamber. AAV particles are retained while other cellular components (*e.g.*, proteins) are passing through the SPE matrix. A wash step is performed to remove non-AAV residues. AAV particles are eluted at low pH, dissociating capsids from the sdAb affinity ligands. The eluted sample is stabilized for downstream use (or storage) before it is recovered from the cartridge. (b) Configuration of the microfluidic circuit (top view). Reservoirs are assigned as follows: (R1) collection chamber; (R2) EqB; (R3) DB; (R4) NB; (R5) EqB; (R6) EB; (R7 and R8) transfer reservoirs to aliment the capture chamber. Passage across the capture unit proceeds horizontally (left to right or right to left). (c) Schematic (3D and cross-sectional view) of the capture unit. (d) Photograph of an assembled cartridge (lower section). The capture chamber is filled with POROS™ CaptureSelect™ AAVX Affinity Resin. The capacity of reservoirs R7 and R8 is about 500 µL each; processing of larger volumes is possible by subsequently transferring smaller aliquots from the vial onto the cartridge. Scale bar: 5 mm.

Nümbrecht, Germany) were used as external vials. The cap of each tube was pierced to accommodate two pieces of SILASTIC™ Laboratory Tubing (0.030″ ID, 0.065″ OD; Dow Corning, Midland, MI). The interface around each tubing was sealed with UV-curable glue.

### 2.3 Production of AAV samples

HEK293SF-3F6 cells were used for AAV production employing a three-plasmid transfection system comprised of pAAV2/8 rep/cap (GeneMedi, Shanghai, China), pAAV2/2 rep/cap, pHelper and the transgene expression cassette (Cell Biolabs, San Diego, CA). Transfections were performed using PEIpro® transfection reagent (Polyplus, Illkirch-Graffenstaden, France). Transfected cells were harvested 72 h post-transfection. AAV lysis was performed as previously described.[34] Briefly, lysing buffer concentrate 1% (v/v) (200 mM $MgCl_2$, 1% Triton X-100) and Benzonase® nuclease 1% (v/v) at 2.5 U $mL^{-1}$ (Merck, Darmstadt, Germany) were added and incubated for 2 h at 37 °C under agitation. Subsequently, $MgSO_4$ (Merck) was added to a final concentration of 37.5 mM and incubated for 30 min.

### 2.4 On-chip AAV purification

The integrated AAV purification process was conducted on a centrifugal platform as described in more detail below. Solutions were pipetted into storage reservoirs (through dedicated pressure ports, as depicted in Fig. S4) prior to securing the cartridge on the rotating stage. The platform was operated using a LabVIEW interface (National Instruments, Austin, TX) which allows for automating the assay through scripts customized according to the requirements of the protocol.[24,26]

### 2.5 Manual AAV purification

A packed bed of bead slurry was formed on a commercial spin column (QIAGEN, Hilden, Germany) from which the original fiber-based extraction matrix had been removed. 100 µL of bead slurry diluted 1 : 10 (v/v) in 0.1 M NaCl solution was pipetted onto the support structure of the spin column, followed by centrifugation using a MiniSpin® Plus (Eppendorf, Hamburg, Germany). Manual AAV purification was performed with the same solutions and volumes as were used for the on-chip purification process. Centrifugation was conducted at 800 rpm for binding followed by washing at 800 rpm. The sample was eluted at 800 rpm using 100 µL of elution buffer (EB). Conditioning of the sample was performed by manually adding equilibration buffer (EqB), neutralization buffer (NB) and dilution buffer (DB), followed by shortly subjecting the vial to vortex agitation.

### 2.6 Vector titration

Crude AAV8 lysates were purified by iodixanol gradient ultracentrifugation (Optima L-80 XP ultracentrifuge; Beckman Coulter, Brea, CA), and vector genome titers were quantified by ddPCR using the QX200 system (Bio-Rad, Hercules, CA).[34]

AAV2 infectious titer was determined by a transduction assay using recombinant AAV2 expressing green fluorescent protein (rAAV2-GFP).[35]

### 2.7 Quantification of pcDNA3-EGFP plasmid

Crude AAV8 samples were spiked with 1 μL of purified pcDNA3-EGFP (enhanced green fluorescent protein) plasmid at 24.9 ng $\mu L^{-1}$ (Addgene, Watertown, MA). Amplification was performed with 2 μL of purified sample using TaqPath™ qPCR Master Mix (Thermo Fisher Scientific). Probes and primers (Table S3) are targeting the EGFP sequence in pcDNA3. Serial dilutions of plasmid were used to establish a standard curve (Table S4, Fig. S5). Plasmid carry-over in purified samples was calculated by extrapolation from the standard curve equation and removal was calculated based on the initial spike-in concentration.

### 2.8 Imaging and fluorescence measurements

Metrology of machined structures was conducted using a VHX Digital Microscope (KEYENCE, Osaka, Japan). Optical micrographs were acquired using an Eclipse Ti-E inverted microscope (Nikon Instruments, Melville, NY) equipped with an iXon Ultra CCD camera (Andor Technology, Belfast, UK). Particle size analysis was performed using ImageJ software (National Institutes of Health, Bethesda, MD) following procedures that are detailed elsewhere.[31] Transmission electron microscopy (TEM) imaging was performed using an H-7500 electron microscope (Hitachi, Tokyo, Japan) following procedures that were described previously.[35] Flow cytometry was performed using an LSRFortessa™ Cell Analyzer (BD Biosciences, Franklin Lakes, NJ); GFP fluorescence was detected using a 488 nm laser for excitation and a 530/30 bandpass filter for emission. Unaltered cells were used as negative control. Data were analyzed using FACSDiva™ and FlowJo software (BD Biosciences).

### 2.9 Numerical simulations

Numerical simulations were performed using COMSOL Multiphysics® software (Momentum Transport – Porous Media Flow module; Burlington, MA). Uniform flow at a rate of 58 μL $min^{-1}$ has been considered at the inlet and uniform pressure with no viscous stress at the outlet of the capture unit. No-slip boundary conditions have been imposed on all other boundaries. Water with a density of $\rho = 1.0$ g $cm^{-3}$ and dynamic viscosity $\eta = 10^{-3}$ Pa s was implied as a carrier liquid and $\varepsilon = 0.26$ and $k = 4.45 \times 10^{-13}$ $m^2$ have been set as default values for the porosity and permeability of the bead bed, respectively.

## 3 Results and discussion

### 3.1 Microfluidic cartridge

The two-level microfluidic circuit (Fig. 1b, S1 and S6) has been designed such that all steps of the AAV purification protocol can be conducted in a reliable fashion to facilitate automation. The use of pressure-mediated actuation on a rotating platform enables bidirectional flow to be induced by pumping liquid against $\vec{F}_{cf}$. Unlike conventional centrifugal systems, where unidirectional flow makes it necessary to place storage compartments close to the center of rotation, the platform used here allows for distributing reservoirs across the entire footprint of the cartridge. On-chip reservoirs (R1–R8; Table S5) are equipped with exit channels that have an upward orientation, thus confining liquid until needed. Pressure ports—connected to the manifold lid on the platform (Fig. S7)—are used to apply controlled air pressure to these reservoirs and so mediate fluid movement; downstream transfer is achieved by simply pushing liquid toward the destination reservoir.[26,27] With the exception of the two serpentine segments (see below), the width and depth of transfer channels are relatively large (*e.g.*, 568 and 503 μm, respectively) to promote high flow rates (*e.g.*, >50 μL $s^{-1}$) in transfer steps. Furthermore, active pneumatic pumping allows for liquid exchange with external vials, greatly increasing the platform's capacity to accommodate assay components.[26] Here, we use vials (inserted into a dedicated holder on the rotating stage) for storing crude lysate, collecting waste, and retrieving the purified AAV sample, respectively (Table S6). Vials are connected to the cartridge through flexible tubing,[26,30] enabling exchange of liquid with R1 (using A1 and A2), R7 (using A3 and A4) and R8 (using B1 and B2), as illustrated in Fig. S8.

POROS™ CaptureSelect™ AAVX Affinity Resin is comprised of poly(styrene-divinylbenzene) particles modified with single-domain antibody (sdAb) fragments, allowing for purification of multiple AAV serotypes.[10,36] The capture unit accommodating these particles was designed as an add-on component to the fluidic conduit (Fig. 1c and d). The independently fabricated capture unit enabled bead slurry to be introduced without unproductive accumulation of excess liquid inside the microfluidic cartridge (Fig. S3). The SPE matrix is retained using constricted gate structures (25 μm depth) on either side, designed to comply with the particle size distribution of the bead slurry (Fig. S9). The implementation of microfabricated constrictions constitutes an option that we and others have successfully used to confine non-magnetic particles in microfluidic devices.[33,37,38] The capture unit is connected to transit reservoirs R7 and R8, which comprise a deep upper section for receiving larger volumes of liquid, and a shallow lower section for monitoring and regulating the fill level during flow through the capture chamber.

### 3.2 Analysis of flow across the capture chamber

We investigated flow behavior for a capture chamber geometry that diverts from the column-like format typically used for AAV purification (Fig. 2). A simple theoretical analysis was performed by employing the Kozeny–Carman model[39] relating the average velocity $\bar{u}$ of the flow to the applied pressure $\Delta p$ and the permeability $k$ of the bead bed as

$$\bar{u} = \frac{k}{\eta}\frac{\Delta p}{L} \quad (1)$$

where $\eta$ is the dynamic viscosity of the flowing liquid and $L$ is the length of the bead bed in the direction of the flow. In this equation, $k$ is expressed as

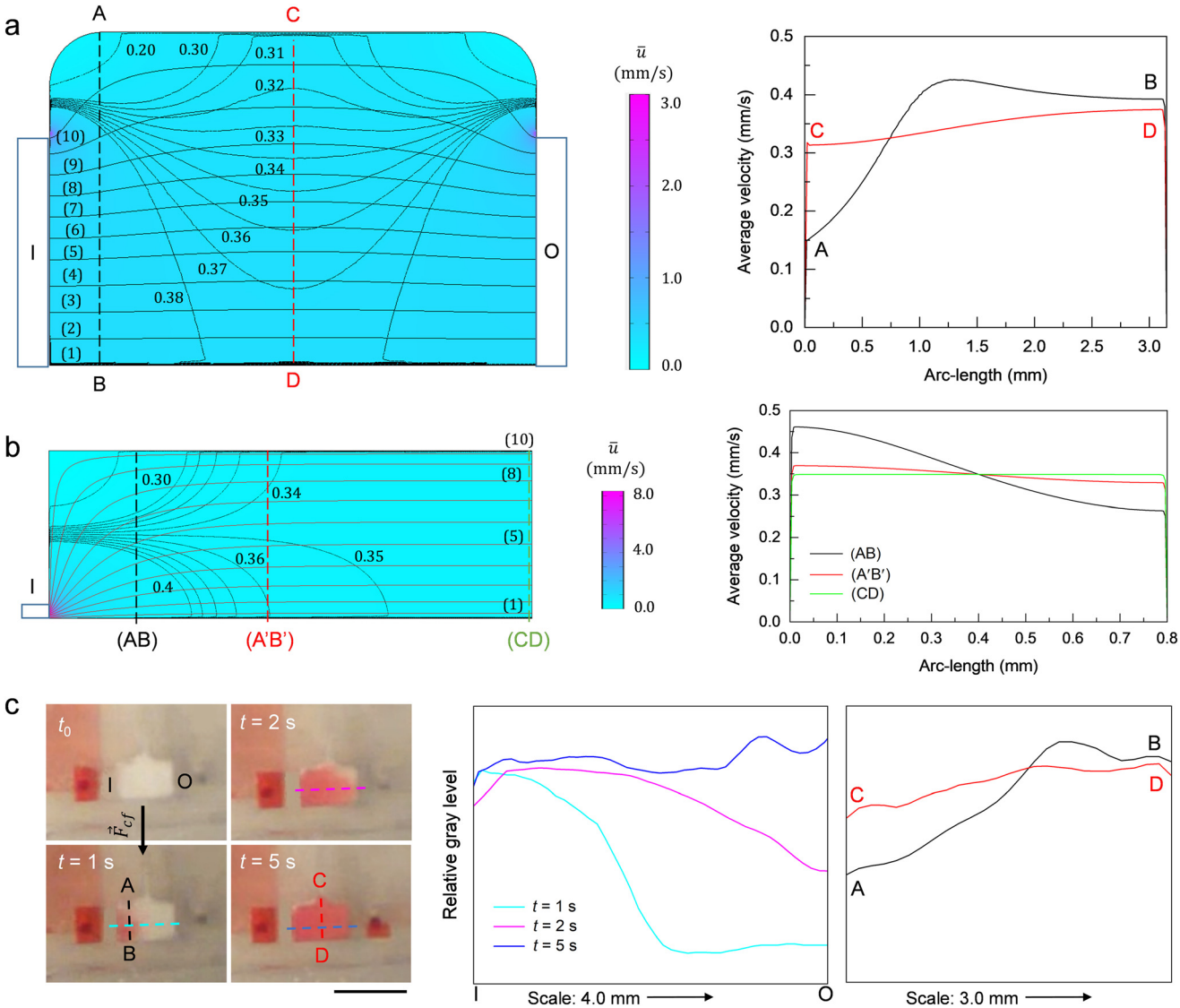


**Fig. 2** Flow across the capture chamber. (a and b) Contour fill plots of the velocity field for in-plane and out-of-plane cross-sections (left-hand panel). The graphs (right-hand panel) show the velocity profiles for different segments of the bead bed. (c) Stroboscopic images (left-hand panel) depicting flow across the bead bed. Aqueous solution containing red-colored dye was used to provide visibility. The platform was rotated at 450 rpm. Scale bar: 5 mm. The graphs show color distribution across the bead bed at different time intervals parallel (IO) and perpendicular (AB, CD) to the flow direction. Signal intensities were subjected to adjacent averaging (5-point window).

$$k = \frac{\varepsilon^3 d_p^2}{180(1-\varepsilon)^2} \quad (2)$$

where $\varepsilon$ is the porosity of the matrix. According to this model, the permeability of a bead bed formed of densely packed monodisperse spherical particles with a diameter ($d_p$) of ~40 μm is determined at $k_0 = 2.85 \times 10^{-13}$ m$^2$. Measurements of the flow rate (for calibrated pressure applied at the pneumatic ports) suggest an apparent experimental value of $k_{exp} = 1.24 \times 10^{-13}$ m$^2$, which is less than half of the theoretical value. This discrepancy can be mainly attributed to the relatively broad range in $d_p$ (*e.g.*, from 20 to 80 μm; Fig. S9).[39] The low aspect ratio of the bead bed and the constrictions retaining the beads in the capture chamber should also contribute to reducing the theoretical value of $k_0$, but their effects have not been taken into account.

According to the Carman theory,[39] the porous bead bed is equivalent to a number $N$ of small channels going in parallel from the inlet (I) to the outlet (O) with an effective length of $L' = 2.5L$ where $L$ is the physical length of the bead bed. The geometry of the bead bed amounts to $N = 11\,466$ rectangular channels of average size $a = 0.48$ μm. The average velocity of the liquid mass transport through the bead bed is $U_0 = Q/A$, resulting in $U_0 = 0.35$ mm s$^{-1}$ for a cross-sectional area $A = 3.67$ mm$^2$, which translates into an average velocity inside the equivalent channels of about $U_0/\varepsilon = 1.3$ mm s$^{-1}$. This means that the transition time (that is, the time spent inside

the bead bed) for the viral vector is about $\Delta t$ = 8.84 s. For this time, the average diffusion length[40]

$$\Delta x \approx \sqrt{6 C_{\mathrm{diff}} \Delta t} \tag{3}$$

is ~30 μm, largely exceeding the average size $a$ of the equivalent rectangular microchannel (and the interstitial void between the beads). Therefore, the probability for viral particles to diffuse away from the streamlines and interact with the SPE matrix is high.

We analyzed the distribution of flow across the bead bed through 2D numerical simulations using the Brinkman equation.[41,42] The simulation results are presented in Fig. 2a and b as velocity profiles for in-plane and out-of-plane cross-sections of the computational domain. The range from 0.2 to 0.4 mm $s^{-1}$ suggests good uniformity of the velocity field landscape and high efficiency in terms of overall surface available for capture. Beads located in corners (for in-plane simulation) and close to the step (for out-of-plane simulation) receive the lowest exposure, but distribution of the sample liquid gradually equilibrates over time as indicated by the evolution of the flow profile from (AB) to (A′B′) and further to (CD). In-plane flow behaviour predicted by the simulation was confirmed experimentally using the real-time imaging capabilities of the platform (Fig. 2c).

### 3.3 On-chip AAV purification process

The microfluidic conduit partitions liquid displacement during the purification process into two primary pathways (Fig. 3a): (i) EqB (from R2) and crude lysate (from vial 2) are directed through the capture unit and subsequently into vial 3; and (ii) EB (from R6) is transferred across the capture unit

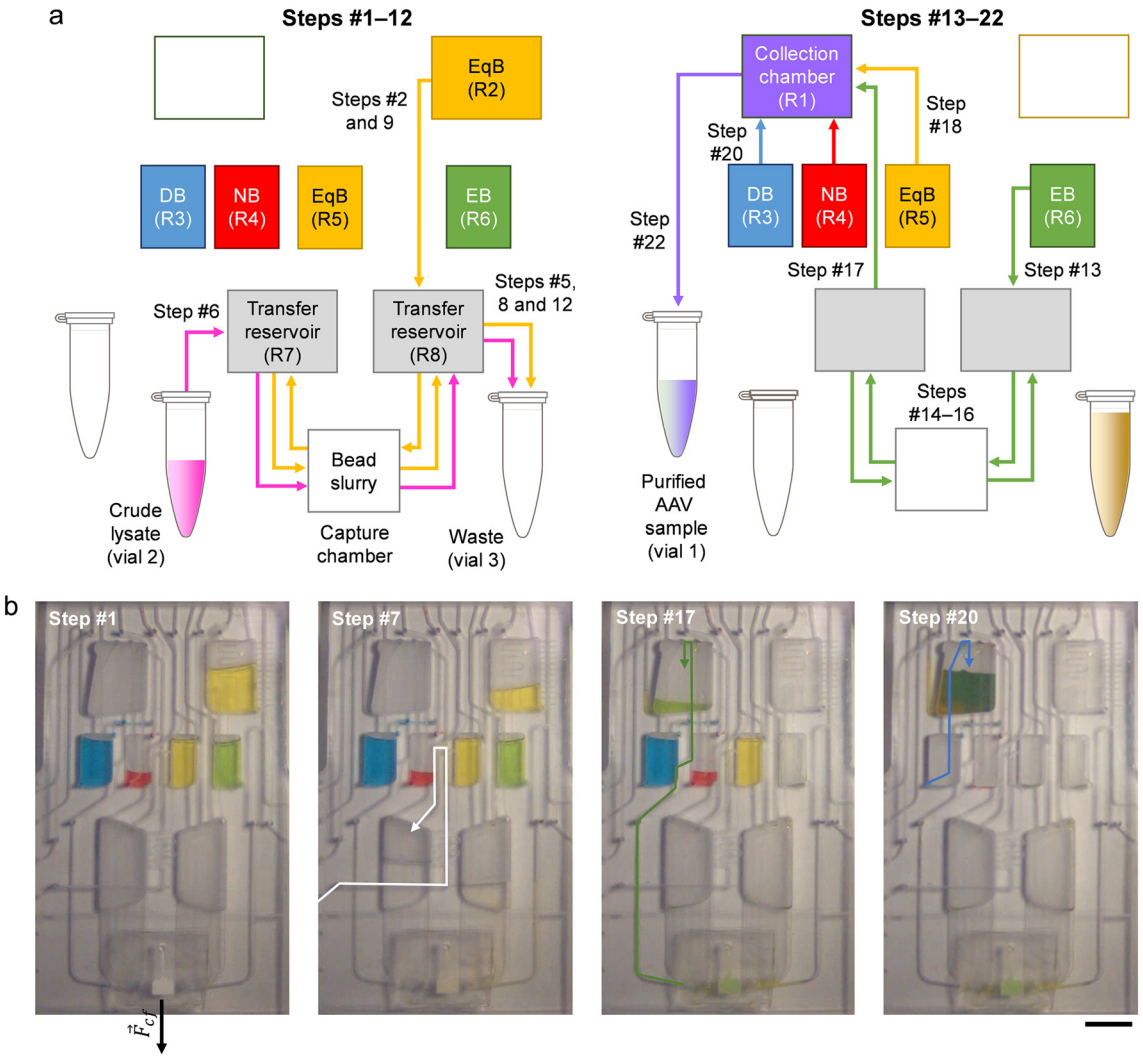


**Fig. 3** Microfluidic AAV purification process. (a) Flow chart detailing connectivity between reservoirs and vials. Arrows indicate the direction of flow. Color coding is used for visual clarity. (b) Stroboscopic images of the cartridge at selected stages of the AAV purification process. Step #1: initiation. Step #7: crude lysate (transferred from vial 2) is flown through the capture chamber. Step #17: eluted sample is transferred from R7 to R1. Step #20: DB is added to R1. During all steps, the cartridge is rotating at 450 rpm in a clock-wise direction with the centrifugal force pointing downward. Solutions were stained with food color dye (except for crude lysate) to enhance visibility and contrast. Scale bar: 1 cm. A video clip of the process is provided in the SI.

**Table 1** Microfluidic protocol

| Step # | Operation[a] | Duration | Applied pressure[b] (psi) | Active ports # |
|---|---|---|---|---|
| 1 | Initiation | 30 s | None | None |
| 2 | Transfer 100 μL of EqB from R2 to R8 | 10 s | +1.5 | 8 |
| 3 | Transfer EqB from R8 to R7 | 40 s | −1.5 | 1, 2, 3, 4, 5, 9, 10 |
| 4 | Transfer EqB from R7 to R8 | 40 s | −1.5 | 6, 7, 8, 11, 12 |
| 5 | Send EqB to vial 3[c] | 5 s | −2 | 12 |
| 6 | Transfer of lysate from vial 2 to R7 | 80 s | +3 | 1 |
| 7 | Transfer lysate from R7 to R8 | 30/60 min[d] | 0 to −0.5 | 6, 7, 8, 11, 12 |
| 8 | Send lysate from R8 to vial 3[c] | 10 s | −2 | 12 |
| 9 | Transfer 100 μL of EqB from R2 to R8 | 20 s | +2 | 8 |
| 10 | Transfer EqB from R8 to R7 | 40 s | −1.5 | 1, 2, 3, 4, 5, 9, 10 |
| 11 | Transfer EqB from R7 to R8 | 40 s | −1.5 | 6, 7, 8, 11, 12 |
| 12 | Send EqB from R8 to vial 3[c] | 5 s | −2 | 12 |
| 13 | Transfer EB from R6 to R8 | 3 s | +2 | 6 |
| 14 | Transfer EB from R8 to R7 | 40 s | −1.5 | 1, 2, 3, 4, 5, 9, 10 |
| 15 | Transfer EB from R7 to R8 | 40 s | −1.5 | 6, 7, 8, 11, 12 |
| 16 | Transfer EB from R8 to R7 | 40 s | −1.5 | 1, 2, 3, 4, 5, 9, 10 |
| 17 | Transfer EB (eluted sample) from R7 to R1[c] | 10 s | +3 | 1, 5, 6, 7, 8, 11, 12 |
| 18 | Transfer EqB from R5 to R1 | 2 s | +2 | 4 |
| 19 | Transfer NB from R4 to R1 | 2 s | +2 | 3 |
| 20 | Transfer DB from R3 to R1 | 2 s | +2 | 10 |
| 21 | Bubble mix solutions in R1 | 5 s | +1 | 9 |
| 22 | Send eluted sample from R1 to vial 1 | 10 s | −3 | 9 |

[a] Performed with the platform rotating at a constant speed of 450 rpm. [b] Relative to atmospheric pressure. [c] Step is repeated since some backflow can occur across the bead bed during initial transfer. [d] 30 min for sample volumes of 50–200 μL and 60 min for 500 μL.

into R1, where it is combined with EqB (from R5), NB (from R4), and DB (from R3) before the sample is collected in vial 1. The integrated workflow (Table 1, Fig. 3b) comprises a timed sequence of pressure actuation steps with the cartridge rotating at a constant speed of 450 rpm (corresponding to ~33 × *g* at the capture chamber).

The bead slurry is first conditioned using one half (*e.g.*, 100 μL) of EqB from R2 (steps #2–5). The constrained serpentine segment in the exit channel enables controlled transfer, accommodating a flow rate of ~10 μL $s^{-1}$ at 450 rpm and an applied pressure of +1.5 psi. The scale on the right-hand side of the reservoir allows for estimating transferred and remaining volumes. Crude lysate is brought onto the cartridge by applying +3 psi to port #1 (step #6). The pressure imbalance created in the vial pushes the lysate into transit reservoir R7 (through another flow rate-adjusting serpentine segment) for downstream extraction (steps #7 and 8). The capture matrix is then washed (steps #9–12) using the remaining half (*e.g.*, 100 μL) of EqB from R2. EB is then transferred from R6 to R8, and slowly moved back and forth through the capture chamber to release AAV particles (steps #13–16). Elution is performed under acidic conditions (*e.g.*, pH 2–3), dissociating AAV capsids from the affinity ligands. To prevent denaturation, eluted samples are immediately neutralized with high pH buffer.[8,36] This is done by transferring eluate from R7 to R1 (step #17), where it is conditioned by subsequently adding EqB, NB and DB, followed by bubble-induced mixing (steps #18–21). For retrieval, negative pressure (*e.g.*, −3 psi) is applied to port #9, thereby aspirating the liquid into vial 1 (step #22). Once the platform is brought to a standstill, the purified AAV sample is recovered from the vial for downstream quality control.

### 3.4 Performance assessment

We validated on-chip purification (Fig. 4) for AAV8 from crude lysate using input volumes of 50, 100 and 500 μL containing $3.88 \times 10^{10}$ viral genomes (vg) per mL. In addition, we conducted a manual purification assay in spin columns to provide a benchmark for comparison. Normalized yield was higher (28% for all data combined) when samples were purified on-chip (Fig. 4a). These findings are consistent with results previously obtained for other purification workflows (*e.g.*, extraction of DNA from blood), where precise temporal control of liquid transfer steps provided by the platform has been shown to improve yield and assay repeatability.[26] The correlation between viral load for input and output samples is displayed in Fig. 4b and c. Smaller aliquots (*e.g.*, 50 and 100 μL) resulted in recovery yields below the theoretical value, while extraction approached 100% yield for 500 μL input samples. Passing lysate multiple times across the capture matrix has been tested as an option to increase extraction yield for smaller input volumes. Using 200 μL aliquots, we demonstrated that the unique capability of the platform to cycle liquid back and forth without loss of sample volume enables an increase in yield of ~0.5% per cycle (Fig. 4d). These observations point to the need for adjusting viral load according to the size of the capture chamber: it is known, for example, that the release of AAV particles can be hampered when conducting purification below the maximum binding capacity of the bead slurry since re-binding events occurring during elution can cause poor recovery yield.[36]

Removal of plasmid was tested using lysate spiked in excess with pcDNA3—a vector used in cell cloning and

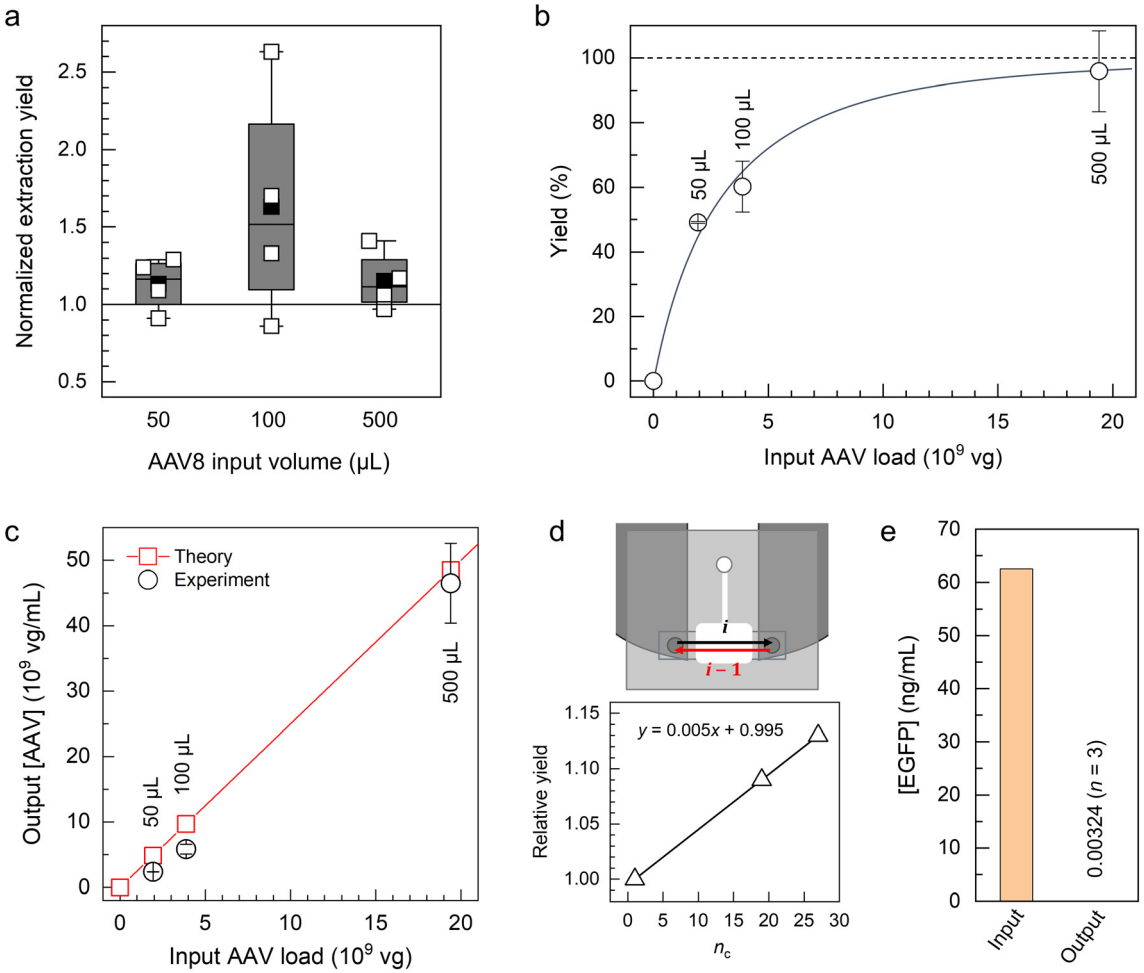


**Fig. 4** Assessment of AAV purification performance. (a) Box plot showing the extraction yield for AAV8pVR59 particles ($3.88 \times 10^{10}$ vg mL$^{-1}$) at different input volumes. White squares: experimental data ($n$ = 4); lower box limit: 25%; upper box limit: 75%; inner line: median; black square: average; error bar: minimum and maximum values. The data was normalized to the yield obtained by manual extraction in spin columns. (b) Plot of extraction efficiency as a function of viral load using 50, 100 and 500 µL sample aliquots ($n$ = 2). The line serves as a guide to the eyes. (c) Plot of AAV concentration for on-chip purification as a function of viral load ($n$ = 2). Theoretical values were included as a reference. (d) Scheme illustrating back and forth movement of sample liquid across the bead bed. The cycle number $n_c$ corresponds to $i + (i - 1)$. The plot shows the effect of $n_c$ on AAV extraction yield (for $i$ = 10 and 14) relative to that obtained by a single passage ($i$ = 1). Experiments were performed using 200 µL of lysate containing AAV8pVR59 particles ($3.88 \times 10^{10}$ vg mL$^{-1}$). The line represents a linear fit of the data set. (e) Plot of EGFP content before and after sample purification. Lysate (500 µL) was spiked with EGFP to provide an input concentration of 62.5 ng mL$^{-1}$.

expression studies—linked to EGFP.[43,44] Purified samples were analyzed using qPCR to quantify plasmid carry-over. Our findings suggest depletion by more than four orders of magnitude (Table S7, Fig. 4e) using one single wash step (100 µL). The fact that residual plasmid is still detectable suggests minor shortcomings in the current cartridge format. One such drawback is related to the size of R2 for which the capacity could be slightly increased to accommodate more buffer solution for rinsing. Another one might be the presence of micro-scale surface roughness in reservoirs and channels as a result of the machining process as well as segments in the fluidic conduit that are prone to retain dead volumes (*e.g.*, vertical steps and corners adjacent to the capture unit). Streamlining the design and adopting fabrication methods based on thermoforming (*e.g.*, hot embossing) should help alleviate effects deriving from these limitations. The use of surfactants can also be envisaged to limit non-specific binding of plasmid (and viral particles) on the polymer surface.

To demonstrate that viral particles maintain their biological potency, a transduction assay was performed using rAAV2-GFP (Fig. 5a). The GFP gene was transferred to human embryonic kidney (HEK) cells, which are widely used in AAV production due to their susceptibility for transfection and rapid growth under different culture conditions.[35] Viral vectors were diluted with infectious AAV virions to maintain the ratio of GFP-positive cells below 20% and ensure that cells are not transduced with more than one viral particle.[35] The rAAV2-GFP-transduction yield was assessed using flow cytometry (Fig. 5b) by measuring autofluorescence for treated and untreated (control) culture isolates. The ratio of GFP-positive cells (*e.g.*, 14.1%) observed for AAV purified on-chip

 

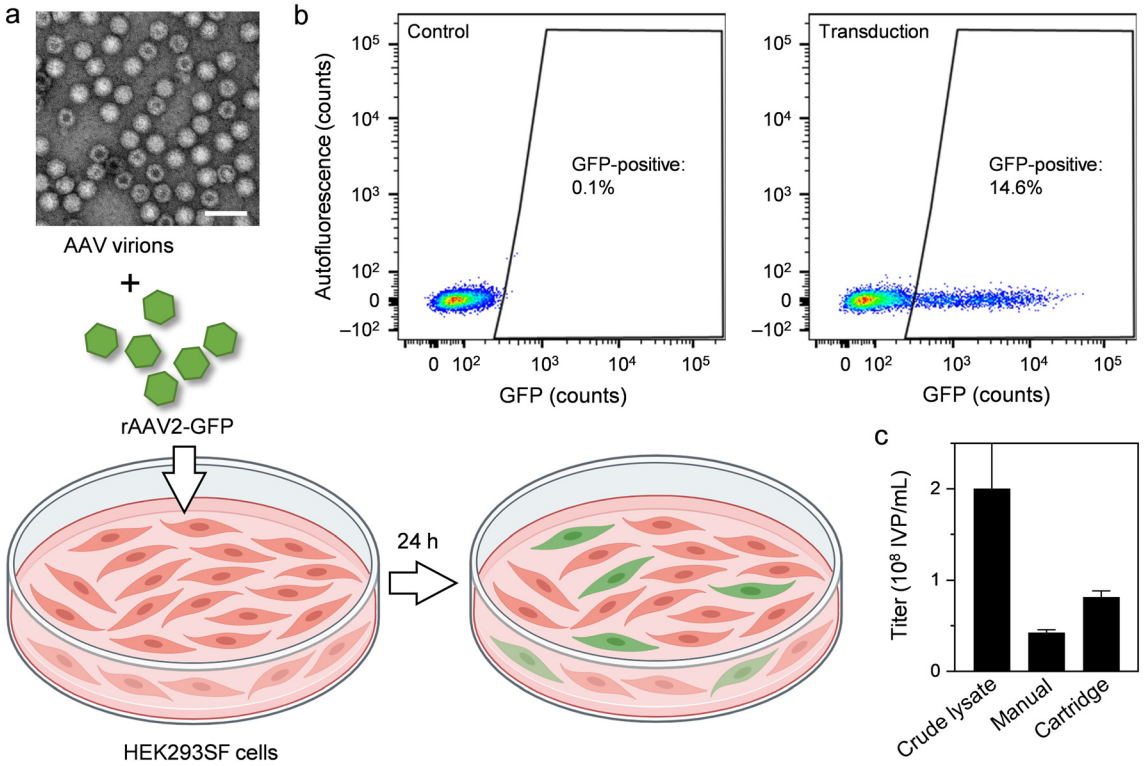


**Fig. 5** Biological activity of purified AAV vectors. (a) Scheme of the transduction process. The TEM image depicts AAV2 virions after purification. Empty capsids are discriminated by their ring-like structure. Scale bar: 50 nm. The scheme was created in part by using templates retrieved from BioRender (https://www.biorender.com). (b) Scatter plots showing GFP fluorescence for unaltered (control) and rAAV2-GFP-transduced HEK293SF cells. (c) Infectious AAV2-GFP titers for purified and non-purified samples as inferred from gene transduction assays ($n$ = 2).

was comparable to that obtained by using iodixanol-purified vectors. Functional titers were calculated in terms of infectious viral particles (IVP per mL).[35] The findings in Fig. 5c confirm that purification conducted on the cartridge results in superior yield compared to the manual process, while also demonstrating that the procedure preserves vector integrity and transduction efficiency.

## 4 Conclusions

We have demonstrated the purification of AAV vectors from crude lysate using a centrifugal microfluidic system amendable to workflow automation for processing sample volumes in the range of 50 to 500 µL. The integrated protocol provides relatively short turn-over times (*e.g.*, 1 h) compared to standard purification based on ultracentrifugation (*e.g.*, 4–5 h), while alleviating potential error associated with performing manipulation steps in a manual fashion. This assay is well suited for crude lysates containing at least ~$20 \times 10^9$ vg in 500 µL loading volume as the binding capacity of the resin is understood to accommodate also partially filled and empty capsids. A higher concentration can always be diluted to meet the 500 µL target volume, if needed. The system in its current configuration allows for operating two cartridges—placed on opposite ends of the rotating stage—in a single run; a higher degree of parallelization can be achieved by upgrading the platform such that a larger number of devices can be accommodated at a time. Reusing the same cartridge constitutes an option that has not been tested here, but should be feasible given that the conditions for cleaning columns prepared from POROS™ CaptureSelect™ AAVX Affinity Resin are well established.[10,36] We believe that the implementation presented in this work can be beneficial for timely monitoring of AAV production yields when optimizing process parameters and accelerating the purification steps in small-scale research and development efforts. Potentially providing detailed insight into purification dynamics under defined conditions, the platform-based approach supports improved process understanding, yield predictability, and early identification of potential bottlenecks. As such, it helps reduce uncertainty and technical (or financial) risk during scale-up, ultimately contributing to more efficient and predictable viral vector manufacturing workflows.

## Author contributions

M. G., L. M., R. G. and T. V. conceptualized the project. L. C., M. G. and D. B. implemented the fluidic design. M. J.-P. and C. M.-G. fabricated and assembled microfluidic cartridges. D. D. F., L. C. and M. G. established the operational protocol. D. D. F. and C. N. conducted manual and on-chip AAV purification experiments. N. N., R. G., N. N.-M., P. S. C. and R. G. produced AAV samples and buffer solutions, and performed vector titration, cell transduction, and related

analysis. C. N. quantified plasmid DNA. L. C. performed numerical simulations. M. G., L. M. and L. C. prepared the figures and tables, and co-wrote the manuscript. N. N., P. S. C., R. G. and T. V. reviewed and edited the text. All authors approved the final version of the manuscript.

## Conflicts of interest

The authors declare no competing financial interest.

## Data availability

The data associated with this study are present in the article or in the supplementary information (SI). Raw data or further experimental details that support the findings of this study can be obtained from the authors upon reasonable request. Supplementary information is available. See DOI: https://doi.org/10.1039/d6lc00382f.

## Acknowledgements

This work was supported by the National Research Council of Canada through the Cell & Gene Therapy Program. We thank our colleagues François Normandin, Aaron Bessoff, Simon Geissbuehler, and Jason Ferreira for technical assistance and useful discussion. We are grateful to Amaya Arcelus for her support.

## References

1 A. Pupo, A. Fernández, S. H. Low, A. François, L. Suárez-Amarán and R. J. Samulski, *Mol. Ther.*, 2022, **30**, 3515–3541.
2 C. Li and R. J. Samulski, *Nat. Rev. Genet.*, 2020, **21**, 255–272.
3 D. Wang, P. W. L. Tai and G. Gao, *Nat. Rev. Drug Discovery*, 2019, **18**, 358–378.
4 J. El Andari and D. Grimm, *Biotechnol. J.*, 2021, **16**, 2000025.
5 T. Kimura, B. Ferran, Y. Tsukahara, Q. Shang, S. Desai, A. Fedoce, D. R. Pimentel, I. Luptak, T. Adachi, Y. Ido, R. Matsui and M. M. Bachschmid, *Sci. Rep.*, 2019, **9**, 13601.
6 P. S. Chahal, E. Schulze, R. Tran, J. Montes and A. A. Kamen, *J. Virol. Methods*, 2014, **196**, 163–173.
7 A. Srivastava, K. M. G. Mallela, N. Deorkar and G. Brophy, *J. Pharm. Sci.*, 2021, **110**, 2609–2624.
8 M. Mietzsch, J. K. Smith, J. C. Yu, V. Banala, S. N. Emmanuel, A. Jose, P. Chipman, N. Bhattacharya, R. McKenna and M. Agbandje-McKenna, *Mol. Ther.–Methods Clin. Dev.*, 2020, **19**, 362–373.
9 S. Shastry, W. Chu, E. Barbieri, P. Greback-Clarke, W. K. Smith, C. Cummings, A. Minzoni, J. Pancorbo, G. Gilleskie, K. Ritola, M. A. Daniele, T. F. Johnson and S. Menegatti, *Biotechnol. J.*, 2024, **19**, 2300230.
10 M. Florea, F. Nicolaou, S. Pacouret, E. M. Zinn, J. Sanmiguel, E. Andres-Mateos, C. Unzu, A. J. Wagers and L. H. Vandenberghe, *Mol. Ther.–Methods Clin. Dev.*, 2023, **28**, 146–159.
11 S. M. Crosson, P. Dib, J. K. Smith and S. Zolotukhin, *Mol. Ther.–Methods Clin. Dev.*, 2018, **10**, 1–7.
12 Y. H. Chen, M. S. Keiser and B. L. Davidson, *Curr. Protoc. Mouse Biol.*, 2018, **8**, e56.
13 E. Dormond, P. Chahal, A. Bernier, R. Tran, M. Perrier and A. Kamen, *J. Virol. Methods*, 2010, **165**, 83–89.
14 O. Strohmeier, M. Keller, F. Schwemmer, S. Zehnle, D. Mark, F. von Stetten, R. Zengerle and N. Paust, *Chem. Soc. Rev.*, 2015, **44**, 6187–6229.
15 E. K. Sackmann, A. L. Fulton and D. J. Beebe, *Nature*, 2014, **507**, 181–189.
16 G. M. Whitesides, *Nature*, 2006, **442**, 368–373.
17 M. Madou, J. Zoval, G. Jia, H. Kido, J. Kim and N. Kim, *Annu. Rev. Biomed. Eng.*, 2006, **8**, 601–628.
18 M. Futami, H. Naito, S. Ninomiya, L. C. Chen, T. Iwano, K. Yoshimura and Y. Ukita, *Biomed. Microdevices*, 2024, **26**, 22.
19 R. Turiello, L. M. Dignan, B. Thompson, M. Poulter, J. Hickey, J. Chapman and J. P. Landers, *Anal. Chem.*, 2022, **94**, 3287–3295.
20 Y. Zhao, Y. Hou, J. Ji, F. Khan, T. Thundat and D. J. Harrison, *Anal. Chem.*, 2019, **91**, 7570–7577.
21 I. Maguire, R. O'Kennedy, J. Ducrée and F. Regan, *Anal. Methods*, 2018, **10**, 1497–1515.
22 E. Duffy, R. Padovani, X. He, R. Gorkin, E. Vereshchagina, J. Ducrée, E. Nesterenko, P. N. Nesterenko, D. Brabazon, B. Paull and M. Vázquez, *Anal. Methods*, 2017, **9**, 1998–2006.
23 O. Strohmeier, S. Keil, B. Kanat, P. Patel, M. Niedrig, M. Weidmann, F. Hufert, J. Drexler, R. Zengerle and F. von Stetten, *RSC Adv.*, 2015, **5**, 32144–32150.
24 M. Geissler, D. Brassard, N. Adam, N. Nasheri, A. V. C. Pilar, K. Tapp, L. Clime, C. Miville-Godin, M. Mounier, C. Nassif, L. Lukic, L. Malic, N. Corneau and T. Veres, *Lab Chip*, 2024, **24**, 668–679.
25 L. Malic, D. Brassard, D. Da Fonte, C. Nassif, M. Mounier, A. Ponton, M. Geissler, M. Shiu, K. J. Morton and T. Veres, *Lab Chip*, 2022, **22**, 3157–3171.
26 D. Brassard, M. Geissler, M. Descarreaux, D. Tremblay, J. Daoud, L. Clime, M. Mounier, D. Charlebois and T. Veres, *Lab Chip*, 2019, **19**, 1941–1952.
27 L. Clime, D. Brassard, M. Geissler and T. Veres, *Lab Chip*, 2015, **15**, 2400–2411.
28 J. Guo, D. Brassard, N. Adam, A. J. Verster, J. A. Shay, C. Miville-Godin, M. Janta-Polczynski, J. Ferreira, M. Mounier, A. V. Pilar, K. Tapp, A. Classen, M. Shiu, D. Charlebois, N. Petronella, K. Weedmark, N. Corneau and T. Veres, *Lab Chip*, 2024, **24**, 182–196.
29 L. Poncelet, K. J. Morton, M. Shiu, G. Veilleux, C. Richer, L. Clime, D. Sinnett and T. Veres, *Lab Chip*, 2026, **26**, 770–782.
30 L. Malic, L. Clime, B.-U. Moon, C. Nassif, D. Da Fonte, D. Brassard, L. Lukic, M. Geissler, K. Morton, D. Charlebois and T. Veres, *Lab Chip*, 2024, **24**, 4755–4765.
31 L. Clime, L. Malic, J. Daoud, L. Lukic, M. Geissler and T. Veres, *Lab Chip*, 2020, **20**, 3091–3095.
32 M. Geissler, L. Clime, X. D. Hoa, K. J. Morton, H. Hébert, L. Poncelet, M. Mounier, M. Deschênes, M. E. Gauthier, G. Huszczynski, N. Corneau, B. W. Blais and T. Veres, *Anal. Chem.*, 2015, **87**, 10565–10572.

 

33 M. Geissler, K. Li, X. Zhang, L. Clime, G. P. Robideau, G. J. Bilodeau and T. Veres, *Lab Chip*, 2014, **14**, 3750–3761.
34 N. Mehta, R. Gilbert, P. S. Chahal, M. J. Moreno, N. Nassoury, N. Coulombe, V. Lytvyn, M. Mercier, D. Fatehi, W. Lin, E. M. Harvey, L.-H. Zhang, N. Nazemi-Moghaddam, S. M. Elahi, C. J. D. Ross, D. B. Stanimirovic and M. R. Hayden, *Hum. Gene Ther.*, 2023, **34**, 927–946.
35 L. Jalšić, V. Lytvyn, S. M. Elahi, S. Hrapovic, N. Nassoury, P. S. Chahal, B. Gaillet and R. Gilbert, *Mol. Ther.–Methods Clin. Dev.*, 2023, **30**, 259–275.
36 *POROS™ CaptureSelect™ AAV Resins: AAV8, AAV9, AAVX User Guide*, Thermo Fisher Scientific, Waltham, MA, 2017, pp. 1–8.
37 K. Boissinot, R. Peytavi, S. Chapdelaine, M. Geissler, M. Boissinot, E. A. Martel, D. Béliveau-Viel, J.-F. Gravel, L. Malic, T. Veres, D. Boudreau and M. G. Bergeron, *Analyst*, 2021, **146**, 4226–4234.
38 E. Hemmig, Y. Temiz, O. Gökçe, R. D. Lovchik and E. Delamarche, *Anal. Chem.*, 2019, **92**, 940–946.
39 P. C. Carman, *Trans. Inst. Chem. Eng.*, 1937, **15**, 150–156.
40 E. A. Codling, M. J. Plank and S. Benhamou, *J. R. Soc. Interface*, 2008, **5**, 813–834.
41 J. Nichele and D. A. Teixeira, *J. Pet. Sci. Eng.*, 2015, **134**, 76–78.
42 H. C. Brinkman, *Appl. Sci. Res.*, 1947, **1**, 27–34.
43 N. Sarkar, R. Mishra, C. Gopal and A. Kumar, *Front. Oncol.*, 2024, **14**, 1411539.
44 A. Prel, C. Dozier, J.-P. Combier, S. Plaza and A. Besson, *Int. J. Mol. Sci.*, 2021, **22**, 3432.